The Astrophysical Journal, 972:63 (8pp), 2024 September 1 https://doi.org/10.3847/1538-4357/ad62ff

Evidence of Gradients of Density and Magnetic Field in the Remnant of Tycho's Supernova

Oleh Petruk[1,2], Taras Kuzyo[2], Mariana Patrii[3], Laura Chomiuk[4], Maria Arias[5], Marco Miceli[1,6], Salvatore Orlando[1], and Fabrizio Bocchino[1]
[1] INAF-Osservatorio Astronomico di Palermo, Piazza del Parlamento 1, 90134, Palermo, Italy
[2] Institute for Applied Problems in Mechanics and Mathematics, Naukova Street 3-b, 79060 Lviv, Ukraine
[3] Faculty of Physics, Ivan Franko National University of Lviv, Kyryla and Methodia 8, 79005 Lviv, Ukraine
[4] Center for Data Intensive and Time Domain Astronomy, Department of Physics and Astronomy, Michigan State University, East Lansing, MI 48824, USA
[5] Leiden Observatory, Leiden University, PO Box 9513, 2300 RA, Leiden, The Netherlands
[6] Dipartimento di Fisica e Chimica E. Segrè, Università degli Studi di Palermo, Piazza del Parlamento 1, 90134, Palermo, Italy
Received 2024 May 20; revised 2024 July 4; accepted 2024 July 11; published 2024 August 26

Abstract

By using surface brightness maps of Tycho's supernova remnant (SNR) in radio and X-rays, along with the properties of thermal and synchrotron emission, we have derived the postshock density and magnetic field (MF) strength distributions over the projection of this remnant. Our analysis reveals a density gradient oriented toward the northwest, while the MF strength gradient aligns with the Galactic plane, pointing eastward. Additionally, utilizing this MF map, we have derived the spatial distributions of the cutoff frequency and maximum energy of electrons in Tycho's SNR. We further comment on the implications of these findings for interpreting the gamma-ray emission from Tycho's SNR.

Unified Astronomy Thesaurus concepts: Supernova remnants (1667); Interstellar medium (847); Interstellar magnetic fields (845)

1. Introduction

The remnant of Tycho's supernova (SN1572, G120.1+1.4) is observed at all wavelengths of the electromagnetic spectrum and marks the site of a Type Ia supernova that appeared in 1572 (Krause et al. 2008). Cosmic rays are accelerated in Tycho's supernova remnant (SNR) to high energies (Morlino & Caprioli 2012). The availability of a significant amount of observational data over the past decades makes this object one of the most interesting research targets.

Multiple radio and X-ray observations indicate that the expansion of the remnant into the interstellar medium (ISM) is anisotropic (Reynoso et al. 1997; Katsuda et al. 2010; Williams et al. 2016; Tanaka et al. 2021). The expansion parameter $(\Delta R/\Delta t)/(R/t)$ for the forward shock radius R in Tycho's SNR varies between 0.2 and 0.8 as measured in radio or X-rays (Reynoso et al. 1997; Katsuda et al. 2010). Thus, there should be irregularities in the ISM density that cause such variations in the proper motion of the shock.

There have been multiple attempts to identify an interaction between the remnant and dense clouds in its vicinity by considering stronger shock deceleration (Reynoso et al. 1999; Lee et al. 2004; Zhou et al. 2016; Chen et al. 2017) or by measuring density variations around the shock front, which could be interpreted as the presence of local ISM gradients (Vigh et al. 2011; Williams et al. 2013). There are a number of studies that have addressed the distribution of dense molecular material around the location of Tycho's SNR (Reynoso et al. 1999; Lee et al. 2004; Cai et al. 2009; Ishihara et al. 2010; Xu et al. 2011; Chen et al. 2017).

Spatially resolved X-ray spectroscopy enables detailed ejecta velocity measurements from Doppler shifts in the source's emission lines (Hayato et al. 2010; Sato & Hughes 2017; Millard et al. 2022; Godinaud et al. 2023; Uchida et al. 2024). It also reveals asymmetries in the expansion of Tycho's SNR and allows us to constrain the ejecta structure.

Little is known about the interstellar magnetic field (ISMF) structure in the remnant's surroundings. Several authors impose limits on the magnetic field (MF) strength in the remnant based on observational data (e.g., Cassam-Chenaï et al. 2007; Wilhelm et al. 2020; Reynolds et al. 2021). Radio and X-ray polarization studies (Reynoso et al. 1997; Ferrazzoli et al. 2023) indicate a predominantly radial MF orientation with an amplification/compression factor of about 3.4 at the shock front.

Three-dimensional magnetohydrodynamic (MHD) simulations of SNR evolution are necessary for a better understanding of the SNR structure, the physical processes related to the supernova explosion and its expansion into a nonuniform ISM, and for testing hypotheses about the cosmic ray acceleration and its high-energy emission. There are several hydrodynamic (HD) or MHD models of Tycho's SNR that aim to explain its observational features as well as azimuthal asymmetries (Chiotellis et al. 2013; Williams et al. 2017; Fang et al. 2018; Ferrand et al. 2019; Moranchel-Basurto et al. 2020; Kobashi et al. 2024). The structure of the ISM density and the MF are crucial inputs for MHD models. Indeed, the ISM density is one of the key factors affecting the SNR shock wave dynamics. On the other hand, the MF is crucial for the nonthermal emission from SNRs and for the cosmic ray acceleration. It could be important, too, during the interaction of the remnant with the circumstellar medium or ISM inhomogeneities. It can also damp HD instabilities that can fragment the inhomogeneities after the shock passage.

Furthermore, the MF is responsible for the (partial) suppression of thermal conduction (Orlando et al. 2008).

The goal of this paper is to provide observation-based evidence for the large-scale gradients in both ISM density and ISMF strength that have direct implications for the evolution of Tycho's SNR. As a next step, we produce images of the distribution of the cutoff frequency and the maximum energy of electrons over the SNR.

2. Observations and Data Reduction

We have used the 1.4 GHz map produced by Williams et al. (2016) from Karl G. Jansky Very Large Array (VLA) observations of Tycho's SNR. The data were taken in 2013–2014 from a combination of A, B, C, and D configurations, observed under project code VLA/13A-426 (PI J. W. Hewitt). Data from two spectral windows covering 1314–1442 GHz were used to image the SNR using uniform weighting. The resulting *L*-band map has a resolution of 1.″91 and a pixel size of 0.″4.

The X-ray maps in the photon energy ranges 1.2−4.0, 4.1−6.0, and 3.0−6.0 keV are derived from Chandra data taken in 2015 (obsid 15998). They were analyzed with the Chandra Interactive Analysis of Observations v.4.12 software. The data were reprocessed with `chandra_repro`, and X-ray maps were produced with the `fluximage` script. The derived X-ray maps have a resolution and pixel size of 0.″492. The radio and X-ray images are taken at almost the same epoch, and therefore no correction is needed to account for the SNR expansion between the observations. The FITS files of the X-ray images are reprojected to the same pixel grid as the radio map to allow for a pixel-to-pixel analysis. This is done by using the flux-conserving function `reproject_exact` from the `astropy` library.

For the spatial variation of the radio spectral index α, we have used the 40″ map derived by Arias et al. (2019). It was made by combining LOw Frequency ARray (van Haarlem et al. 2013) data at 48.3, 67.0, and 144.6 MHz with VLA data at 327 MHz (Katz-Stone et al. 2000) and 1382 MHz (Williams et al. 2016). The spectral index map was produced by, for each pixel, fitting for a value of the flux density, spectral index, and line-of-sight absorption. The spectra index α (where flux density $S_\nu \propto \nu^{-\alpha}$) varies in value from 0.55 to 0.75 over the surface of Tycho's SNR. The pixel size in the the spectral index map is larger than in the radio and X-ray maps. Therefore, we prescribed the same radio spectral index for all pixels in our grid that correspond to a single one in the spectral index image.

3. Results

3.1. Density and MF Strength

Our goal is to understand the large-scale distribution of the density and MF strength around Tycho's SNR. We have adopted our method for processing maps of SNRs in different photon energy ranges (Petruk et al. 2009). The basic idea is to derive images of the global distribution of density and MF strength over Tycho's SNR resulting from the evolution of the plasma inside (including both following components: the swept-up ISM and the ejecta) after impact with the ambient medium.

The synchrotron radio emissivity is

$$\epsilon_{\rm r} \propto KB^{(s+1)/2}, \tag{1}$$

where $K \propto n$ is the normalization of the electron spectrum, $s = 2\alpha + 1$, α is the radio index, n is the number density, and B is the MF strength of the component in the plane of the sky. The surface brightness in each pixel of an image is the sum of the emissivity along the line of sight inside the SNR.

We can write the radio brightness in each pixel as

$$q_{\rm r} \propto \eta_{\rm r} n B^{(s+1)/2}, \tag{2}$$

where $\eta_{\rm r}$ is a geometrical factor, different for the different pixels in the image. It accounts for the distribution of the radio emission along the line of sight inside the SNR.

The thermal X-ray emissivity is

$$\epsilon_{\rm x} \propto n^2 \Lambda(T, \tau), \tag{3}$$

where $\Lambda(T, \tau)$ is a cooling function for an optically thin plasma with temperature T and ionization state is characterized by the parameter τ. Tycho's SNR is a young object with a high shock speed V (average $V \approx 3300\,{\rm km\,s^{-1}}$ for distance $d = 2.3$ kpc) and high postshock electron temperatures $T > 10^7$ K (Williams et al. 2013). For the thermal X-ray map, we use the X-ray data in the photon energy range 1.2−4 keV, where the function $\Lambda(T)$ is approximately constant for such temperatures and different ionization states (Appendix). If this is the case, then the surface brightness in each pixel of the image is approximately

$$q_{\rm x} \propto \eta_{\rm x} n^2, \tag{4}$$

where $\eta_{\rm x}$ is a geometrical factor for the thermal X-ray emission.

Equation (4) yields the following density distribution over the SNR projection:

$$n \propto (q_{\rm x}/\eta_{\rm x})^{1/2}. \tag{5}$$

The expression for the MF map over the SNR follows from Equations (2) and (4):

$$B \propto \left(\frac{q_{\rm r}^2}{q_{\rm x}}\frac{\eta_{\rm x}}{\eta_{\rm r}^2}\right)^{1/(s+1)}. \tag{6}$$

By using n from Equation (2) in Equation (4) we assume the same injection efficiency for electrons in the forward and reverse shocks. Differences in density between the shocked ISM and the ejecta material are reflected in the geometrical factors, which account for the internal structure of the remnant.

The geometrical factors $\eta_{\rm r}$, $\eta_{\rm x}$ vary from pixel to pixel. They may be estimated from geometrical considerations and the internal profiles of emissivity for the SNR. Namely, we use the Abel inversion:

$$\eta(\bar{r}) = 2\int_{\bar{r}}^{1} \bar{f}\,(r')\frac{r'dr'}{\sqrt{r'^2 - \bar{r}^2}}, \tag{7}$$

where $\bar{r} = r/R$, r is the distance from the explosion point, R is the SNR radius, and $\bar{f}\,(r) = f(r)/f_{\rm s}, f_{\rm s} \equiv f(R)$ is the postshock value of the function $f(r)$, which represents the spatially variable part of the emissivity. We adopt the functions $f_{\rm r} = nB^{3/2}$ for the radio band and $f_{\rm x} = n^2$ for the thermal X-rays. They are calculated using $n(r)$ and $B(r)$ from numerical simulations, namely, with the radial density and MF profiles for the remnant of an SN Ia explosion at age

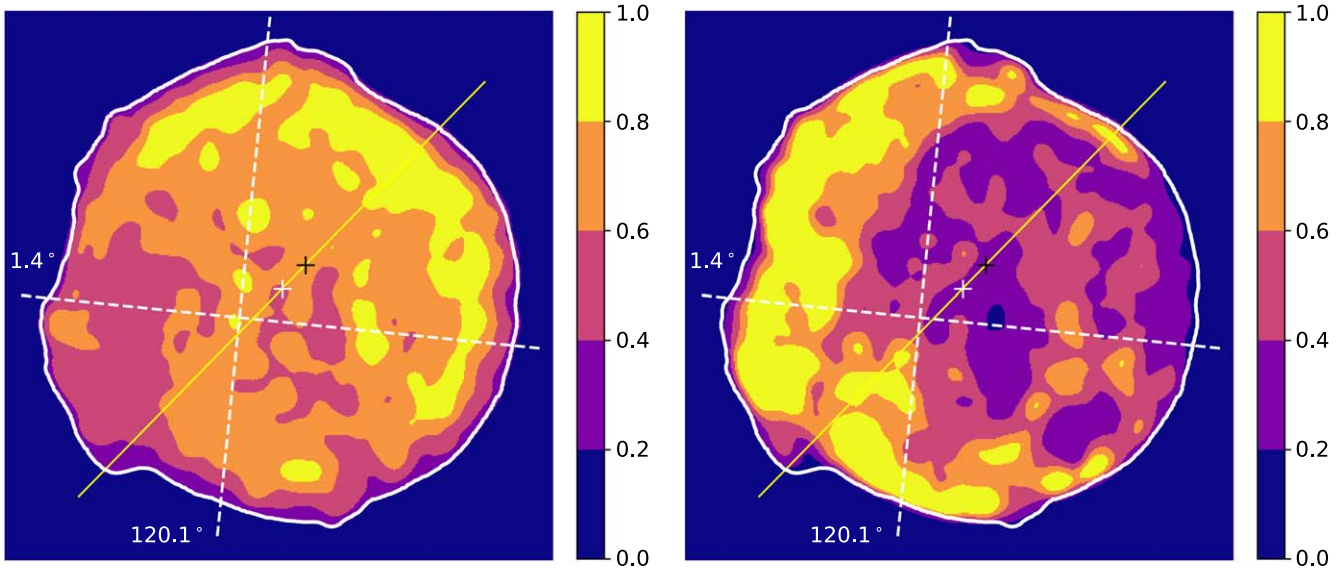

Figure 1. Left: density distribution derived from the thermal X-ray image of Tycho's SNR and Equation (5). Right: distribution of MF strength derived from the radio and thermal X-ray images of Tycho's SNR and Equation (6). The color scales are in arbitrary units. The outer contour of the SNR (white line) is produced from the radio image. The white cross corresponds to the geometrical center of the SNR, while the black one corresponds to the actual location of the explosion. The yellow line passes through the two centers. The white dashed lines mark Galactic coordinates $l = 120.^{\circ}1$, $b = +1.^{\circ}4$. The Galactic plane is located below the remnant. The grid of equatorial coordinates is parallel to the edges of each figure; north is on top, east on the left. Both images (with size 1500 × 1500 pixels) are smoothed with a Gaussian ($\sigma \approx 20$ pixels) to reduce small-scale fluctuations.

450 yr from our one-dimensional MHD simulations (Petruk et al. 2021). It appears that $\eta_r \approx \eta_x$ for $\bar{r} = 0.75 - 1$ (numerically, they are in the range 0.20−0.36) and differ from one another by about 30% for smaller radii $\bar{r} < 0.75$ (with values between 0.12 and 0.20). We apply these radial functions $\eta_r(\bar{r})$ and $\eta_x(\bar{r})$ for different azimuths by scaling them with their respective R for each direction from the explosion center. We take the coordinates of the SN center from Xue & Schaefer (2015). Note that η is determined by using a normalization to the postshock values ($\bar{r} = r/R$, $\bar{f} = f/f_s$). Therefore, Equations (5) and (6) for the density and MF strength give not the average values along the line of sight but rather the postshock values of n and B.

The derived images for the postshock number density and the postshock MF strength in Tycho's SNR are shown in Figure 1. There are also two centers shown on these plots: the geometrical center (which corresponds to the circular fit of the outer edge of the SNR; Warren et al. 2005; Katsuda et al. 2010) and the actual center (estimated from the backward extrapolation of the proper motion vectors for different filaments; Xue & Schaefer 2015).

3.2. Cutoff Frequency and Maximum Energy of the Electrons

Once we have the map of the MF, we may apply a procedure similar to one used in the `srcut` spectral fitting model in `XSPEC` and consider the particle acceleration. We use the fluxes at the radio ν_r and the X-ray ν_x frequencies as well as the radio spectral index to reconstruct the broadband synchrotron emission of the radiating electrons.

Tycho's SNR is a young object. The maximum energy of the electrons E_{max} is likely limited by its age rather than radiative losses. A good proxy for the particle distribution in energy, in this case, is a power law with an exponential cutoff. The accurate approximation to the synchrotron spectrum corresponding to such a model is given by Equation (8) in Petruk et al. (2009):

$$\epsilon_{xs} = \epsilon_r \left(\frac{\nu_x}{\nu_r}\right)^{-(s-1)/2} \exp\left[-\beta_x \left(\frac{\nu_x}{\nu_{cr}}\right)^{0.364}\right], \quad (8)$$

where $\nu_{cr} = c_1 B E_{max}^2$ is the cutoff frequency (i.e., the critical frequency for the electrons with the maximum energy), $\beta_x = 1.46 + 0.15 \cdot (2 - s)$, $c_1 = 6.26 \times 10^{18}$ cgs, and ϵ_{xs} refers to the X-ray synchrotron emission.

We have to account for the following geometrical factors when applying this relation to the maps: $q_r = \eta_r \epsilon_r$ and $q_{xs} = \eta_{xs} \epsilon_{xs}$. It is known that the length scale for the radial distribution of the X-ray emitting electrons is shorter than for the radio-emitting particles. The synchrotron X-ray emission is from electrons with energies around E_{max}. Therefore, their normalized density $\bar{n} = n/n_s$ downstream of the shock is about e times smaller compared to the normalized density of electrons with a power-law spectrum. Thus, the geometrical factor for the synchrotron X-rays is $\eta_{xs} \simeq e^{-1} \eta_r$. By solving Equation (8) for the cutoff frequency, we have

$$\nu_{cr} \simeq \nu_x \left(\frac{1}{\beta_x} \ln\left[\frac{\eta_{xs} q_r}{\eta_r q_{xs}} \left(\frac{\nu_r}{\nu_x}\right)^{(s-1)/2}\right]\right)^{-2.75}. \quad (9)$$

We use $\nu_r = 1.4 \times 10^9$ Hz, $\nu_x = 1 \times 10^{18}$ Hz (corresponding to 4.1 keV), and for q_{xs}, the hard X-ray image of Tycho's SNR in the 4.1−6 keV range.

The definition of the critical frequency gives the following expression to produce the map of the maximum energy of electrons from the maps of B and ν_{cr}:

$$E_{max} = \left(\frac{\nu_{cr}}{c_1 B}\right)^{1/2}. \quad (10)$$

The image of MF $\bar{B}$ on Figure 1 is in normalized units. In order to convert it to physical units B, we calculate the mean

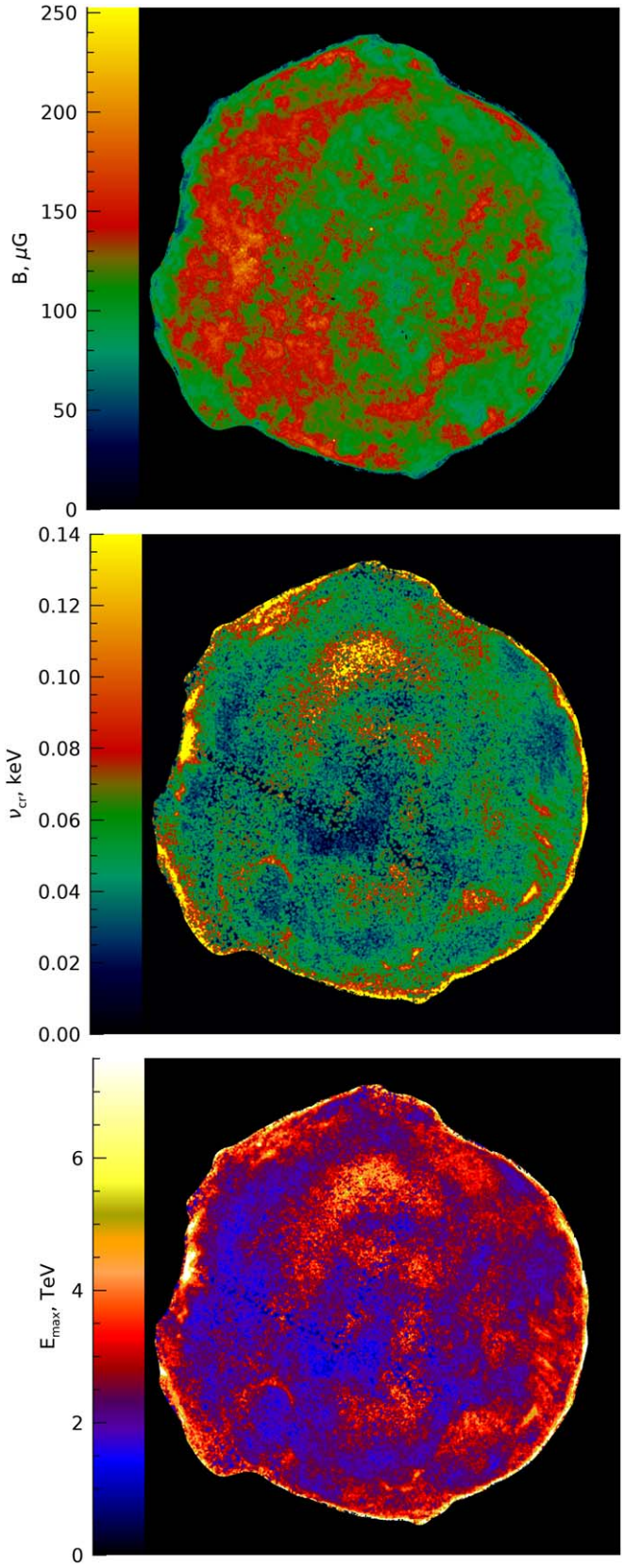

Figure 2. Top: MF strength B. The distribution of values of B is close to a Gaussian with 120 ± 23 μG. Center: cutoff photon energy $h\nu_{cr}$ derived from observational data with Equation (9). Bottom: maximum energy of electrons E_{max} as given by Equation (10).

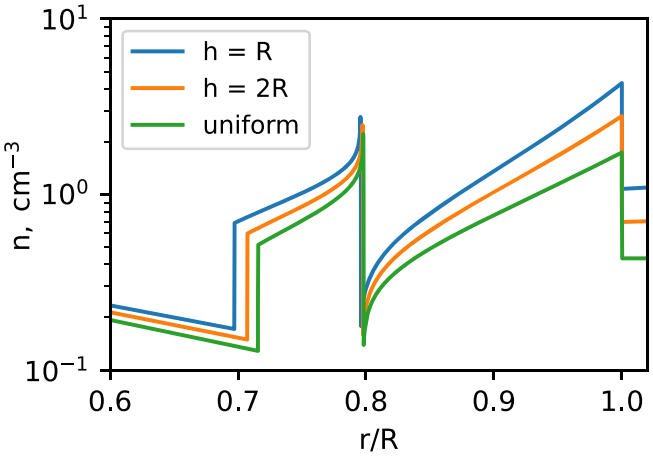

Figure 3. Density profiles corresponding to the remnants of an explosion in an ISM with density distribution (11) with $h = R$ and $h = 2R$, compared to the case of a uniform ISM density n_o = const. R is the SNR radius in the constant n_o. The profiles correspond to an age of 450 yr and are the result of one-dimensional numerical simulations for an initial ejecta structure corresponding to SN Ia (see details in Petruk et al. 2021).

value of the MF strength in normalized units $\langle \bar{B} \rangle$ and assume that this value corresponds to the mean field in the remnant $\langle B \rangle = 120$ μG. Figure 2 (top) shows the map of the MF where each pixel has strength $B = \bar{B} \cdot \langle B \rangle / \langle \bar{B} \rangle$. We see from this figure that the mean value that we adopted provides $B \simeq 200$ μG in the regions along the SNR rim; this value coincides with that estimated by other authors (Reynolds et al. 2021, and references therein). Thus, we substitute Equation (10) with B calculated in this way.

The images in Figure 2 show the distribution of the cutoff frequency and the maximum energy of the electrons over Tycho's SNR obtained with this approach.

Although synchrotron emission dominates in the regions around the edge of the SNR (Lopez et al. 2015), thermal emission also contributes to the total flux in the hard X-rays. In order to be certain in our results, we calculate ν_{cr} by also considering the synchrotron-to-thermal X-ray fraction κ. By utilizing Chandra and IXPE observations, Ferrazzoli et al. (2023) derived the synchrotron fraction map for the 3–6 keV photons over Tycho's SNR. In this photon energy range, the value of κ varies from 0.16 to 0.90 across the SNR (their Figure 7). We have used this map by setting $q_{xs} = \kappa q_{xh}$, where q_{xh} corresponds to the observed X-ray map in 3−6 keV. The images of ν_{cr} and E_{max} derived in this way are the same as in Figure 2 with a slightly lower resolution due to the structure of the map for κ.

4. Discussion and Conclusions

4.1. Gradients of Density and MF Strength

We have already noted at the end of Section 3.1 that our density and MF maps were derived in such a way to give the postshock values of n and B. Although the ejecta material considerably contributes to the thermal X-ray emission in Tycho's SNR, the left map on Figure 1 shows the large-scale distribution of the ambient density. The density of the shocked ejecta reflects the large-scale structure of the ISM because the flow structure adapts to the ambient conditions. Figure 3 shows

the profiles of the density behind a shock evolving in an ISM with density

$$n_{\rm o}(r) = n_{\rm o}(0)\exp(r/h), \quad (11)$$

where r is the distance from the explosion center and h the scaling factor for the nonuniformity. Indeed, the ejecta density (between 0.7 and 0.8 r/R) is higher in the case of a stronger gradient. Another piece of information from this plot is that the different profiles are quite similar and may be scaled. This provides a justification for our procedure to use the geometrical factors η.

We have previously studied how the nonuniformity of interstellar density and interstellar MF affects the thermal X-ray (Hnatyk & Petruk 1999) and nonthermal radio (Orlando et al. 2007), X-ray, and gamma-ray (Orlando et al. 2011) morphologies of SNRs. Comparing Figure 1 with the general properties revealed in these references, we may come to the following conclusions about gradients.

It is apparent from Figure 1 (left) that the density is higher in the northwest region. The yellow line is plotted to pass through the two centers (white and black crosses). It appears to mark the symmetry axis for the density distribution in Tycho SNR. In fact, this property provides strong evidence for the presence of a large-scale density gradient in the ISM around Tycho's SNR, which is directed toward the northwest, along the yellow line. Theoretical studies demonstrate (Hnatyk & Petruk 1999) that the actual center of the SNR should be shifted with respect to the geometrical one in the direction of the gradient of the ambient density. Thus, our figure is an independent confirmation of the explosion center found by Xue & Schaefer (2015).

There is "direct" evidence for a preshock density variation around Tycho SNR. One piece of evidence comes from proper motion analysis of the forward shock in Tycho's SNR on the basis of radio observations (Reynoso et al. 1997). Figure 7 in this reference shows the azimuthal variation of the expansion parameter $m = (\Delta R/\Delta t)/(R/t)$. As from this study, m marks prominent shock deceleration—due to the interaction with increased density—in the northwestern direction. This is the same as the direction of the density gradient we found.

In the same study, the parameter m also demonstrates a strong shock deceleration toward the east, along the azimuth $\approx 70^\circ$ (counterclockwise from the north). A considerable decrease of the expansion velocity at this azimuth is confirmed by X-ray data as well (Williams et al. 2016). Analysis of infrared observations reveals a prominent increase of the preshock density in both the northwestern and eastern directions (Williams et al. 2013).

In contrast, our map in Figure 1 does not reflect a density enhancement toward the east. Our method does not "measure" the density around the shock. It instead relies on the internal distributions. Therefore, the difference between the two azimuths should be due to different spatial scales of the corresponding overdensities and timescales of interactions. The one toward the northwest is large scale (larger than the SNR radius). Therefore, the SNR evolved throughout its entire life in an ISM with this gradient, and the internal structure of the SNR has had enough time to adapt to such an ambient density variation. In contrast, the density enhancement on the east should be localized, and the interaction with the shock is small scale. According to our interpretation, the shock has encountered it rather recently, so the downstream structure does not reflect this interaction yet, unlike the shock itself.

Recent deceleration of the shock at azimuth $\approx 70^\circ$ is confirmed by the analysis of the proper motion of the forward shock from multiepoch X-ray observations between the years 2003 and 2015 (Tanaka et al. 2021; their region 4). The authors found as well a prominent gradual decrease of the shock speed for the south and southwestern edge of Tycho's SNR (their regions 6–10; azimuths $150^\circ - 270^\circ$). There is a sign of such a behavior (namely, smaller m) around the azimuth 180° in Figure 7 in Reynoso et al. (1997). Tanaka et al. (2021) interpreted this as evidence of a recent interaction with a denser cavity wall. However, there is no excessive postshock density found in the infrared 2004 data in the south and southwest (Williams et al. 2013) that could result in such a rapid deceleration. Thus, in the scenario proposed by Tanaka et al. (2021), the southwest portion of the shock should start interaction with a higher-density feature in more recent times than the eastern portion around the azimuth 70° because the overdensity at this azimuth is visible in the infrared data.

Figure 1 (right) demonstrates that the MF map in Tycho's SNR has an arch-like feature. In case of a uniform ambient MF, the MF configuration in the SNR is expected to be barrel like due to a higher compression of the tangential MF component compared to the radial one. The MF projection would then have two symmetric limbs. Such an arch-like configuration in Tycho's SNR could appear if, e.g., the two limbs are slanted toward the east and converging there. Such a configuration (Orlando et al. 2007, 2011) may naturally happen if the gradient of the ambient MF is directed toward the east and it is just swept up and compressed by the shock. Instead, if such a young SNR still has significant amplification of the MF around the forward shock, then one would expect that the MF upstream is approximately either

$$\delta B^2 \propto n_{\rm o} V^3 \quad (12)$$

for nonresonant amplification or

$$\delta B^2 \propto B_{\rm o} n_{\rm o}^{1/2} V \quad (13)$$

for the resonant case. The compression of such a disordered MF by the shock is independent of its obliquity. Thus, in the first case, we expect the MF map to look similar to the density map, which is not the case for ours, or to be dominated by the regions with the highest shock speed V, which are neither those on the northwest or east. The resonant amplification case could in principle result in an MF map as in Figure 2 if the ordered ambient B dominates the azimuthal variation of density and shock speed.

The symmetry axis of the MF distribution seems parallel to the white dashed line running from the west to the east (which indicates Galactic latitude $b = +1.^\circ 4$). Therefore, the ISMF gradient around Tycho's SNR is parallel to the Galactic plane. Interestingly, such orientation differs from the orientation of the MF gradient in the remnant SN1006, where it is directed toward the Galactic plane (Bocchino et al. 2011).

We have no observational clues regarding the orientation of the ambient MF. The radio and X-ray polarization maps reveal a mostly radial MF inside the SNR projection (Reynoso et al. 1997; Ferrazzoli et al. 2023). This is a young SNR, and the generation of a turbulent MF should be efficient. Such an MF component can considerably change the MF direction

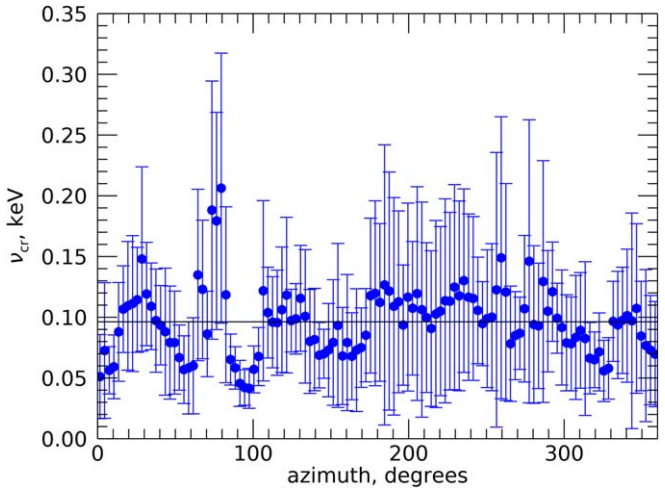

Figure 4. Mean and standard deviation of ν_{cr} around the SNR edge. The azimuth is measured counterclockwise from the north. Each point on the plot is calculated with the data from a region limited by a 3° sector and 5% extension inward along a radius from the edge. The black horizontal line shows the mean value for the whole rim (within 5% of the radius).

compared to what we may expect in the case of a simple compression of the interstellar field.

To summarize, it looks like the ambient environment around Tycho's SNR has the large-scale gradients of the density in the northwest direction and of the MF, which is oriented toward the east and is almost parallel to the Galactic plane.

4.2. Cutoff Frequency and Maximum Energy of the Electrons

The electrons emitting X-rays suffer from radiative losses. They lose energy rather quickly, and the synchrotron X-ray rims of SNRs are therefore thin. We see this clearly in the distributions of the cutoff frequency and the maximum energy in Figure 2. The highest values are around the SNR edge, with a trend to somewhat larger cutoff frequencies and maximum energies in the western half of the remnant's rim.

The azimuth variation of the cutoff frequency around the SNR edge is plotted in Figure 4 for angular bins of 3°. One of the most prominent enhancements is in the region of the recent shock–cloud interaction around azimuth 70°. The local values reach up to $\nu_{cr} \simeq 0.42$ keV and $E_{max} \simeq 11$ TeV at this location. The variation of the cutoff frequency in other regions is typically within 50% of the mean value for the whole rim, with evidence for values systematically above the mean in the western part of the shell (azimuth from 180° to 290°; Figure 4).

Lopez et al. (2015) measured the cutoff frequency by fitting the NuSTAR spectrum in several regions over the remnant. Their Figure 10 shows features similar to ours: in the interior, ν_{cr} is generally smaller by a factor of ≈2.5 compared to the rim; it is higher over the western rim and locally in the east. They estimated, by assuming a uniform MF, that E_{max} varies spatially in the range of 5−12 TeV. Parizot et al. (2006) estimated an MF strength of $B \approx 200\ \mu$G from rim thickness as well as a maximum energy of electrons $E_{max} \simeq 5$–7 TeV. These numbers agree with our calculations (bottom of Figure 2).

On both our maps (for ν_{cr} and E_{max}; Figure 2), we see higher values also around well-known nonthermal features such as the stripes at the west ($E_{max} \simeq 4.0$ TeV) and the arch in the southeast region ($E_{max} \simeq 3.7$ TeV) that prove efficient energization of particles there. The overall distribution of the maximum energy in our image is characterized by a mean $E_{max} = 2.6$ TeV and a standard deviation of 0.9 TeV. It is $E_{max} = 4.0 \pm 1.7$ TeV for the rim.

4.3. On the Gamma-Ray Emission

Tycho's SNR was detected in GeV (Giordano et al. 2012) and TeV (Acciari et al. 2011) gamma-rays. Hadronic gamma-rays arise from regions with a high density of target protons. There are two preferable locations in the case of Tycho's SNR, where the shock is interacting with denser ISM (Williams et al. 2013): in the northwest (in the direction of the large-scale gradient) and in the east (around azimuth 70°).

Neither VERITAS nor Fermi can resolve the object to distinguish between the two locations. Indeed, the centroid position for the TeV gamma-ray emission is in the middle of the line between the two sites (Acciari et al. 2011; their Figure 1). In the GeV gamma-rays, the centroid is around the center of SNR (Giordano et al. 2012; Archambault et al. 2017), i.e., it is also between the two sites.

Our results could shed some light on differences in particle acceleration and gamma-ray emission at these two locations. The shock speed V in the northwest is around 3400 km s^{-1} and near 2000 km s^{-1} in the east (Williams et al. 2013). One would expect to have more efficient acceleration of cosmic rays in the northwest because of the higher shock speed. However, it follows from our results that V measured in the east got smaller recently and sharply, in contrast to the northwest where the shock was decelerating continuously from early times due to increasing ambient density. Before the encounter with the dense material in the east, the shock speed could be as high as the highest V in Tycho (which is around 4000 km s^{-1}; the same reference). The fact that E_{max} for the electrons is higher in the east (being achieved before the sharp decrease of the shock speed due to a recent interaction with an overdensity) than in the northwest (where the shock speed was lower for a long time) confirms such a scenario (bottom of Figure 2). Thus, we would favor the eastern region as the major site contributing to the gamma-ray flux: cosmic rays were accelerated efficiently at the fast shock there and then "suddenly" hit the cloud with a high density of target protons. This supports the scenario of particle acceleration in a shock interacting with dense medium described by Morlino & Blasi (2016).

Acknowledgments

We are thankful to Adam Foster for the valuable suggestions related to usage of the AtomDB data in numerical calculations as well as to Riccardo Ferrazzoli who provided us with the synchrotron fraction map for Tycho SNR. This paper employs a list of Chandra data sets, obtained by the Chandra X-ray Observatory, contained in DOI:10.25574/cdc.259. O.P. acknowledges the OAPa grant No. D.D.75/2022 funded by Direzione Scientifica of Istituto Nazionale di Astrofisica, Italy. L.C. is grateful for support from National Science Foundation grants AST-2107070 and AST-2205628. This project has received funding through the MSCA4Ukraine project, which is funded by the European Union. Views and opinions expressed are, however, those of the authors only and do not necessarily reflect those of the European Union. Neither the European Union nor the MSCA4Ukraine Consortium as a whole nor any individual member institutions of the MSCA4Ukraine Consortium can be held responsible for them. The National Radio

Astronomy Observatory is a facility of the National Science Foundation operated under cooperative agreement by Associated Universities, Inc. This work made use of the HPC system MEUSA, part of the Sistema Computazionale per l'Astrofisica Numerica (SCAN) of INAF-Osservatorio Astronomico di Palermo, Italy.

Appendix
Cooling Function in the Photon Energy Range 1.2–4.0 KeV

In order to get rid of the dependence of the cooling function Λ on the temperature and ionization state of the plasma, we adopt the photon energy range 1.2–4 keV. Figure 5 left shows $\Lambda(T)$ for collisional ionization equilibrium (CIE) as well as for nonequilibrium ionization (NEI) for a few values of the ionization parameter $\tau \equiv n_{\rm o} t$. In order to calculate the plot, we have used the `PyAtomDB` code (https://pypi.org/project/pyatomdb/) with the abundance, which is the default in `XSPEC`. It is evident that $\Lambda(T) \approx$ const for $T > 10^7$ K as in the CIE and NEI conditions. The maximum possible differences in Λ due to local conditions are less than a factor of 2 (green and red lines on the figure). For reference, typical values of τ in Tycho SNR are $\tau \sim 2 \times 10^8$ cm^{-3} s for thin regions of swept-up ISM around the forward shock and $\tau \sim (0.3-1) \times 10^{11}$ cm^{-3} s in the ejecta behind (Decourchelle et al. 2001; Hwang et al. 2002; Ellien et al. 2023).

What could be an effect of spatial variation of abundance? The lines from Si and S are most prominent in the X-ray spectrum of Tycho SNR in the photon energies 1.2–4 keV. These two elements almost coincide spatially. Based on XMM-Newton observations of the remnant, Miceli et al. (2015) derived the equivalent width map for Si, which is a good proxy for its abundance (right of Figure 5). This map demonstrates that variation of Si abundance is at most to the factor of 2 over the remnant. This is the same level of uncertainty as due to τ.

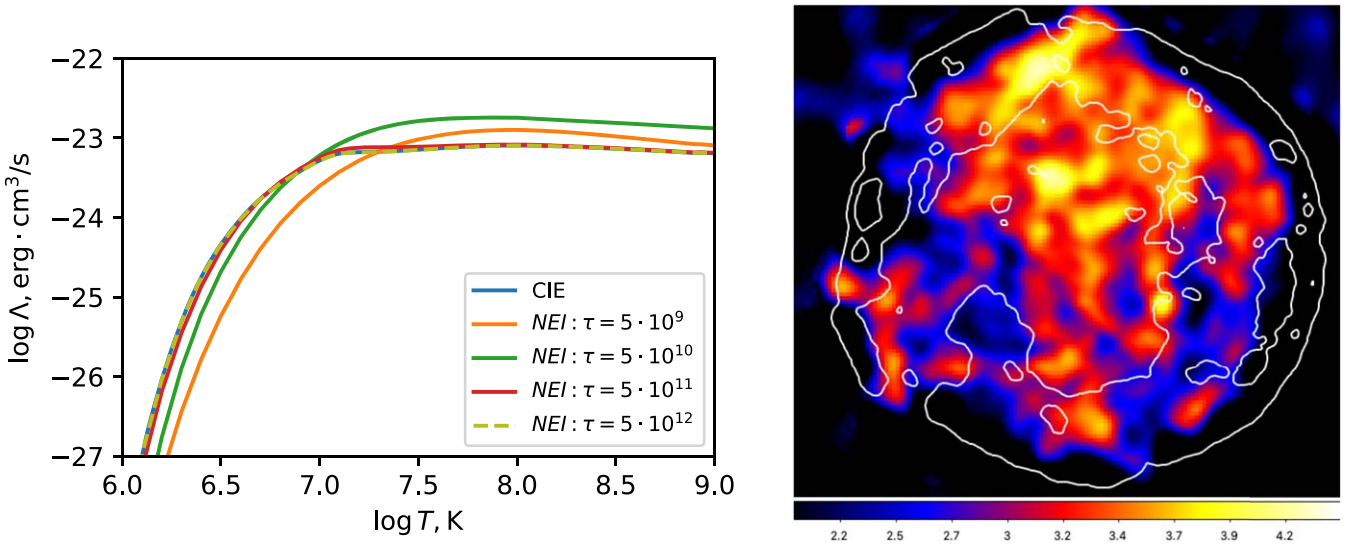

Figure 5. Left: the dependence $\Lambda(T)$ in the photons with energy 1.2−4.0 keV. CIE (blue line) and NEI with values of τ are shown in the legend. The line for $\tau = 5 \times 10^{12}$ cm^{-3} s almost coincides with the CIE line. Right: equivalent width map for the Si emission lines in the 1.65−2.05 keV band. The color scale is in keV. The contours correspond to the map in 4.4−6.1 keV and are plotted at the levels 10% and 30% of the maximum.

ORCID iDs

Oleh Petruk https://orcid.org/0000-0003-3487-0349
Taras Kuzyo https://orcid.org/0000-0001-8464-0360
Mariana Patrii https://orcid.org/0000-0002-3226-3118
Laura Chomiuk https://orcid.org/0000-0002-8400-3705
Maria Arias https://orcid.org/0000-0002-7918-904X
Marco Miceli https://orcid.org/0000-0003-0876-8391
Salvatore Orlando https://orcid.org/0000-0003-2836-540X
Fabrizio Bocchino https://orcid.org/0000-0002-2321-5616

References

Acciari, V. A., Aliu, E., Arlen, T., et al. 2011, ApJL, 730, L20
Archambault, S., Archer, A., Benbow, W., et al. 2017, ApJ, 836, 23
Arias, M., Vink, J., Zhou, P., et al. 2019, AJ, 158, 253
Bocchino, F., Orlando, S., Miceli, M., & Petruk, O. 2011, A&A, 531, A129
Cai, Z.-Y., Yang, J., & Lu, D.-R. 2009, ChA&A, 33, 393
Cassam-Chenaï, G., Hughes, J. P., Ballet, J., & Decourchelle, A. 2007, ApJ, 665, 315
Chen, X., Xiong, F., & Yang, J. 2017, A&A, 604, A13
Chiotellis, A., Kosenko, D., Schure, K. M., Vink, J., & Kaastra, J. S. 2013, MNRAS, 435, 1659
Decourchelle, A., Sauvageot, J. L., Audard, M., et al. 2001, A&A, 365, L218
Ellien, A., Greco, E., & Vink, J. 2023, ApJ, 951, 103
Fang, J., Yu, H., & Zhang, L. 2018, MNRAS, 474, 2544
Ferrand, G., Warren, D. C., Ono, M., et al. 2019, ApJ, 877, 136
Ferrazzoli, R., Slane, P., Prokhorov, D., et al. 2023, ApJ, 945, 52
Giordano, F., Naumann-Godo, M., Ballet, J., et al. 2012, ApJL, 744, L2
Godinaud, L., Acero, F., Decourchelle, A., & Ballet, J. 2023, A&A, 680, A80
Hayato, A., Yamaguchi, H., Tamagawa, T., et al. 2010, ApJ, 725, 894
Hnatyk, B., & Petruk, O. 1999, A&A, 344, 295
Hwang, U., Decourchelle, A., Holt, S. S., & Petre, R. 2002, ApJ, 581, 1101
Ishihara, D., Kaneda, H., Furuzawa, A., et al. 2010, A&A, 521, L61
Katsuda, S., Petre, R., Hughes, J. P., et al. 2010, ApJ, 709, 1387
Katz-Stone, D. M., Kassim, N. E., Lazio, T. J. W., & O'Donnell, R. 2000, ApJ, 529, 453
Kobashi, R., Lee, S.-H., Tanaka, T., & Maeda, K. 2024, ApJ, 961, 32
Krause, O., Tanaka, M., Usuda, T., et al. 2008, Natur, 456, 617
Lee, J.-J., Koo, B.-C., & Tatematsu, K. 2004, ApJL, 605, L113
Lopez, L. A., Grefenstette, B. W., Reynolds, S. P., et al. 2015, ApJ, 814, 132
Miceli, M., Sciortino, S., Troja, E., & Orlando, S. 2015, ApJ, 805, 120
Millard, M. J., Park, S., Sato, T., et al. 2022, ApJ, 937, 121
Moranchel-Basurto, A., Velázquez, P. F., Ares de Parga, G., et al. 2020, MNRAS, 494, 1531
Morlino, G., & Blasi, P. 2016, A&A, 589, A7
Morlino, G., & Caprioli, D. 2012, A&A, 538, A81
Orlando, S., Bocchino, F., Reale, F., Peres, G., & Pagano, P. 2008, ApJ, 678, 274
Orlando, S., Bocchino, F., Reale, F., Peres, G., & Petruk, O. 2007, A&A, 470, 927
Orlando, S., Petruk, O., Bocchino, F., & Miceli, M. 2011, A&A, 526, A129
Parizot, E., Marcowith, A., Ballet, J., & Gallant, Y. A. 2006, A&A, 453, 387
Petruk, O., Bocchino, F., Miceli, M., et al. 2009, MNRAS, 399, 157
Petruk, O., Kuzyo, T., Orlando, S., Pohl, M., & Brose, R. 2021, MNRAS, 505, 755
Reynolds, S. P., Williams, B. J., Borkowski, K. J., & Long, K. S. 2021, ApJ, 917, 55
Reynoso, E. M., Moffett, D. A., Goss, W. M., et al. 1997, ApJ, 491, 816
Reynoso, E. M., Velázquez, P. F., Dubner, G. M., & Goss, W. M. 1999, AJ, 117, 1827
Sato, T., & Hughes, J. P. 2017, ApJ, 840, 112
Tanaka, T., Okuno, T., Uchida, H., et al. 2021, ApJL, 906, L3
Uchida, H., Kasuga, T., Maeda, K., et al. 2024, ApJ, 962, 159
van Haarlem, M. P., Wise, M. W., Gunst, A. W., et al. 2013, A&A, 556, A2
Vigh, C. D., Velázquez, P. F., Gómez, D. O., et al. 2011, ApJ, 727, 32
Warren, J. S., Hughes, J. P., Badenes, C., et al. 2005, ApJ, 634, 376
Wilhelm, A., Telezhinsky, I., Dwarkadas, V. V., & Pohl, M. 2020, A&A, 639, A124
Williams, B. J., Borkowski, K. J., Ghavamian, P., et al. 2013, ApJ, 770, 129
Williams, B. J., Chomiuk, L., Hewitt, J. W., et al. 2016, ApJL, 823, L32
Williams, B. J., Coyle, N. M., Yamaguchi, H., et al. 2017, ApJ, 842, 28
Xu, J.-L., Wang, J.-J., & Miller, M. 2011, RAA, 11, 537
Xue, Z., & Schaefer, B. E. 2015, ApJ, 809, 183
Zhou, P., Chen, Y., Zhang, Z.-Y., et al. 2016, ApJ, 826, 34